European Journal of Nuclear Medicine and Molecular Imaging
https://doi.org/10.1007/s00259-021-05447-4

ORIGINAL ARTICLE

A radioiodinated FR-β-targeted tracer with improved pharmacokinetics through modification with an albumin binder for imaging of macrophages in AS and NAFL

Xuejun Wen[1] · Changrong Shi[1] · Liu Yang[2] · Xinying Zeng[1] · Xiaoru Lin[1] · Jinxiong Huang[3] · Yesen Li[3] · Rongqiang Zhuang[1] · Haibo Zhu[2] · Zhide Guo[1] · Xianzhong Zhang[1]

Received: 4 March 2021 / Accepted: 3 June 2021

Abstract

Purpose The formation of advanced plaques, which is characterized by the uninterrupted aggregation of macrophages with high expression of folate receptor-β (FR-β), is observed in several concomitant metabolic syndromes. The objective of this study was to develop a novel FR-β-targeted single-photon emission computed tomography (SPECT) radiotracer and validate its application to the noninvasive detection of atherosclerosis (AS) plaque and non-alcoholic fatty liver (NAFL).

Methods Two radioiodinated probes, [^{131}I]IPBF and [^{131}I]IBF, were developed, and cell uptake studies were used to identify their specific targets for activated macrophages. Biodistribution in normal mice was performed to obtain the pharmacokinetic information of the probes. Apolipoprotein E knockout (ApoE$^{-/-}$) mice with atherosclerotic aortas were induced by a high-fat and high-cholesterol (HFHC) diet. To investigate the affinity of radiotracers to FR-β, K_d values were determined using in vitro assays. In addition, the assessments of the aorta in the ApoE$^{-/-}$ mice at different stages were performed using in vivo SPECT/CT imaging, and the findings were compared by histology.

Results Both [^{131}I]IPBF and [^{131}I]IBF were synthesized with > 95% radiochemical purity and up to 3 MBq/nmol molar activity. In vitro assay of [^{131}I]IPBF showed a moderate binding affinity to plasma proteins and specific uptake in activated macrophages. The prolonged blood elimination half-life ($t_{1/2z}$) of [^{131}I]IPBF (8.14 h) was observed in a pharmacokinetic study of normal mice, which was significantly longer than that of [^{131}I]IBF ($t_{1/2z}$ = 2.95 h). As expected, the K_d values of [^{131}I]IPBF and [^{131}I]IBF in the Raw 264.7 cells were 43.94 ± 9.83 nM and 61.69 ± 15.19 nM, respectively. SPECT imaging with [^{131}I]IPBF showed a high uptake in advanced plaques and NAFL. Radioactivity in excised aortas examined by ex vivo autoradiography further confirmed the specific uptake of [^{131}I]IPBF in high-risk AS plaques.

Conclusions In summary, we reported a proof-of-concept study of an albumin-binding folate derivative for macrophage imaging. The FR-β-targeted probe, [^{131}I]IPBF, significantly prolongs the plasma elimination half-life and has the potential for the monitoring of AS plaques and concomitant fatty liver.

Keywords Folate receptor-β · Activated macrophage · Atherosclerosis · Albumin binding · Molecular imaging

Abbreviations

AS	Atherosclerosis
FR-β	Folate receptor-β
NAFL	Non-alcoholic fatty liver
PET	Positron emission tomography
SPECT	Single-photon emission computed tomography
CVD	Cardiovascular disease
HSA	Human serum albumin
HPLC	High-performance liquid chromatography
Ox-LDL	Oxidized-LDL
ORO	Oil red O
FA	Folic acid
MWCO	Molar weight cutoff
WT	Wild type
HFHC	High fat and high cholesterol
ApoE$^{-/-}$	Apolipoprotein E knockout
SMA	Smooth muscle actin

This article is part of the Topical Collection on Preclinical Imaging

✉ Zhide Guo
gzd666888@xmu.edu.cn

✉ Xianzhong Zhang
zhangxzh@xmu.edu.cn

Extended author information available on the last page of the article

Published online: 21 June 2021

%IA/g	Percentage of injected activity per gram
ROIs	Regions of interest
H&E	Hematoxylin-eosin

Introduction

Early detection of atherosclerosis (AS)-associated inflammation can reduce the morbidity and mortality associated with cardiovascular events and influence the final clinical outcomes.[1–3] Growing evidence has confirmed the close connection between coronary AS and non-alcoholic fatty liver (NAFL).[4] Previous studies have confirmed that patients with fatty liver are more likely to develop AS over time [5, 6]; On the other hand, cardiovascular disease (CVD) risk factors can predict the occurrence of NAFL, suggesting a bi-directional connection between NAFL and AS. [7] Therefore, combining NAFL with early AS will better predict CVD risk than traditional cardiovascular risk factors alone.

Fortunately, molecular imaging techniques, including positron emission tomography (PET) and single-photon emission computed tomography (SPECT), are increasingly used in CVD diagnosis, and they can effectively detect AS and NAFL with high sensitivity and specificity. Therefore, nuclear medicine imaging using specific targeted probes offered novel possibilities for understanding molecular events that underlie coronary plaque and steatosis formation and has great potential to become a meritorious tool for early detection of advanced AS [8, 9] and NAFL.[10, 11] It is well known that the composition and inflammatory state of vulnerable plaques are the determinants of most acute CVDs. [12, 13] Experimental and clinical data support a pivotal role for activated macrophages in the progression of AS plaques, destabilization, and clinical complications.[14] During the NAFL formation, the liver macrophages are recruited and activated to a pro-inflammatory phenotype.[15] A study involving Korean young adults indicated that an increase in the $CD68^+$ Kupffer cells (liver-resident macrophages) in biopsy samples accompanied severe NAFL in a patient.[16] Folate receptors (FR) consist of four glycopolypeptide members, including FR-α, FR-β, FR-γ, and FR-δ. Among them, FR-α and FR-β have been widely researched. FR-α is overexpressed in a majority of ovarian cancers, breast cancers, and lung carcinomas, but it has a low and restricted distribution in normal tissues.[17–19] FR-β is highly expressed in activated macrophages but not in resting macrophages.[20] Previous studies have demonstrated that FR-β expression correlates with the presence of CD68, an activated macrophage marker.[21] The upregulation of FR-β-positive macrophages (pro-inflammatory) is a characteristic of aortic plaques that are susceptible to rupture.[22, 23].

Based on the imaging method of PET/SPECT, specifically targeted probes have the potential to detect advanced AS plaques and clinical complications.[24] Radiolabeled folate derivatives (^{18}F-FOL and [^{99m}Tc]Tc-EC20, etc.) have been used to assess FR-β-positive activated macrophages at the site of inflammation, such as myocarditis, AS plaques, and myocardial infarction. [25–28] Those findings indicated that FR-β-targeted molecular imaging could provide an effective approach for the early detection of CVD risk in patients with advancing AS and chronic inflammatory disorders.[20] In previous studies, [29–31] we developed several ^{99m}Tc-labeled folate derivatives with characteristics suitable for tumor imaging. Unfortunately, blood elimination study [32] demonstrated that these small-molecule probes (^{99m}Tc-HYNIC-D_1-FA_2 and ^{99m}Tc-HYNFA) were eliminated quickly, and they could not bind to the FR in the AS plaques effectively. To improve the blood half-life of radiotracers, an FR-targeted versatile two-dimensional Pd@Au nanoprobe for the identification of high-risk AS plaques was developed in our group. [32] The long-circulating and FR-targeted two-dimensional materials offer advantages, including a high specificity, low background interference, enhanced sensitivity, and versatile multimodal imaging. However, some limitations, such as stability and biocompatibility, make the nanoplatform difficult to spread during clinical transformation.

In this study, we developed an albumin-binding FR-specific imaging agent ([^{131}I]IPBF), based on the concept of the albumin binder which is gaining widespread adoption as a reliable strategy for increasing the tumor uptake of radiotracers. [33–37] For comparison, a radioiodinated folate derivative ([^{131}I]IBF) without the albumin binder was synthesized simultaneously. Based on the efficient albumin-binding approach and macrophage-targeted strategy, we found that [^{131}I]IPBF can specifically characterize FR-β expression in AS plaques and NAFL with enhanced imaging contrast, which has the potential to serve a large population of patients with CVD risk and metabolic syndrome factors. Also, the additional value of these albumin-binding installation should be extensively investigated in CVD diagnosis.

Methods

Reagents and instruments

All chemicals were obtained commercially and used without further purification. Human serum albumin (HSA) was purchased from Sigma-Aldrich. $Na^{131}I$ was purchased from HTA Co., Ltd. The radioactivity was measured using a CRC-25R Dose Calibrator (CAPIN-TEC. Inc, USA). Purification and analysis were performed using Dionex Ulti-Mate 3000 high-performance liquid chromatography (HPLC, Thermo Scientific, USA) using a flow-counter radioactivity detector (BioScan, USA). SPECT imaging was performed using a

nanoScan-SPECT/CT preclinical scanner (Mediso, Hungary). Autoradiography was performed using a storage phosphor imager (Cyclone Plus, PerkinElmer Instruments Inc., USA). Immunofluorescence staining was performed using a Zeiss LSM 880 + Airyscan microscope (Carl Zeiss, Germany). Immunohistochemistry results were acquired using a Leica DM4B microscope (Leica, Germany). Flow cytometry was performed using a CyroFlex flow cytometer (Beckman Coulter, USA).

Synthesis and radiolabeling

The [^{131}I]IPBA-NHS and [^{131}I]SIB were synthesized in the presence of Cu_2O and 1,10-phenanthroline according to the procedures described previously. [38] A short PEG linker was used to modify the folic acid (FA) at the γ-carboxylic group with high reactivity to produce FA-PEG-NH_2, which was previously separated and purified from previous studies. [29] The mixture of a radioiodinated iodobenzene derivative ([^{131}I]IPBA-NHS or [^{131}I]SIB, ~ 12 MBq), 100 μg FA-PEG-NH_2, and 5 μL N,N-diisopropylethylamine in 100 μL N,N-dimethylformamide was shaken in an oscillator for 1 h at 37 °C. After radiolabeling, the target products ([^{131}I]IPBF and [^{131}I]IBF) were isolated and prepared by semi-preparative HPLC. The radiochemical purity and stability of the radiolabeled compounds were measured using HPLC. The HPLC conditions were as follows: a linear gradient eluent starting from 50% A (0.1% TFA in water) and 50% B (0.1% TFA in methanol), increasing to 90% B at a flow rate of 1 mL/min for 15 min, remaining constant at 90% B for another 15–30 min.

Octanol/water partition coefficient

To determine the hydrophilicity of [^{131}I]IPBF and [^{131}I]IBF, the octanol/water partition coefficients (log P) were measured. Briefly, 100 μL of [^{131}I]IPBF or [^{131}I]IBF solution was diluted with 0.9 mL PBS and 1 mL 1-octanol. After vortexing for 5 min, the mixtures were centrifuged at 10,000 rpm for 5 min. Subsequently, 100 μL of the organic layer was removed and added to 0.9 mL of 1-octanol and 1 mL of PBS for vortex blending and centrifugation. The process was repeated, and a γ-counter was used to obtain the radioactive counts during the organic and aqueous phases (100 μL), respectively. All experiments were independently repeated three times and reported as the mean ± SD.

Docking study

Molecular docking was performed using Schrödinger software (Version 2019–1). The co-crystal structure of HSA complexed with bicalutamide (PDB ID: 4LA0) was obtained from the PDB database. The protein was prepared using Protein Preparation Wizard to assign bond orders, add hydrogens, add missing atoms, remove the unwanted water, fill in the missing side chains and loops, and adjust the protein. The small molecule was converted from 2 to 3D using the LigPrepmodule with the default options. The OPLS3e force field was used for the energy minimization of protein and ligands. The default parameters in standard precision (SP) mode in the Schrödinger software were used for all molecular docking. The native ligand, bicalutamide, was redocked to the original binding pocket of the protein structure to validate the docking method. The images for the molecular simulation were generated using PyMol.

Albumin-binding properties

The binding affinity of the probe to the HSA was determined as previously described. [38] In brief, a dialysis membrane with a molar weight cutoff (MWCO) of 10 kDa was used. [^{131}I]IPBF or [^{131}I]IBF was added to 5 mL HSA at a concentration of 1 mg/mL and vibrated in an oscillator for 30 min at room temperature. The mixed solution was placed in the dialysis membrane and dialyzed in 1 L PBS (pH = 7.4) to separate the free radiotracer from the HSA. The dialysis solutions (5 mL) were taken out at pre-selected time points, and radioactivity was measured in a γ-counter. The remaining radioactivity of the liquid in the dialysis membrane was measured using a radioactivity calibrator.

The in vitro albumin-binding affinities of [^{131}I]IPBF were measured using a competition assay with [^{127}I]IPBF, which are nonradioactive folate compound. Briefly, [^{131}I]IPBF and increasing concentrations of [^{127}I]IPBF were incubated with HSA for 1 h at 37 °C. After incubation, an ultrafiltration membrane with an MWCO of 10 kDa was used to separate the unconjugated small molecules. Thereafter, the radioactivity bound to HSA in the ultrafiltration centrifuge was measured using a γ-counter. The IC_{50} values were calculated by fitting the data with nonlinear regression using GraphPad Prism 7.0. Experiments were performed in triplicate.

The saturation binding study was carried out to measure the binding affinity of radiotracers for HSA. Briefly, HSA was incubated with [^{131}I]IPBF, ranging from 1 to 1000 nM. To determine the non-specific uptake, excess [^{127}I]IPBA (1 mmol/L) was added to block the binding of HSA with radiotracers. After incubation at 37 °C for 1 h, the solutions were added to an ultrafiltration centrifuge tube (10 kDa) to separate unbound radiotracers and washed three times with 0.5 mL of PBS (pH = 7.4). The radioactivity was measured using a γ-counter. The equilibrium dissociation constant (K_d) and the maximum number of binding sites (B_{max}) were calculated using GraphPad Prism software (version 7.0).

Oil red O (ORO) staining and immunofluorescent staining of foam cells

Murine macrophages cells Raw 264.7 cell lines were originally obtained from the Institute of Basic Medicine, Chinese Academy of Medical Sciences, and cultured under recommended conditions. The cells were seeded into 12-well plates at 5.0×10^5 cells per well in RPMI 1640 folate-free medium containing 10% fetal calf serum, and the mixture was maintained at 37 °C in a humidified atmosphere of 5% CO_2. Macrophage activation through oxidized-LDL (ox-LDL) has been proven by Rios et al. [39, 40] The macrophages were incubated with 50 mg/L ox-LDL in RPMI 1640 medium for 24 h to form foam cells. The foam cells were stained with ORO and counterstained with hematoxylin–eosin (H&E). The macrophages were incubated in RPMI 1640 medium without ox-LDL as a control. Subsequently, the cells were photographed using an Olympus microscope.

Similarly, Raw 264.7 cells were pretreated with ox-LDL for 24 h and stained with anti-FOLR2 and anti-CD68 antibodies. Finally, the nucleus was stained with diamidine phenylindole (DAPI). In contrast, ox-LDL-untreated Raw 264.7 cells were stained with the same antibodies and DAPI. Confocal imaging was performed using Olympus FV10-ASW software.

Flow cytometry analysis

Raw 264.7 cells (1×10^6 cells/mL) were inoculated into the 6-well plate overnight. The culture medium was replaced with a fresh RPMI 1640 medium containing 0.3% bovine serum albumin and ox-LDL (50 mg/L), and the mixture was incubated for 24 h. Anti-FOLR2 antibody was used to characterize the FR-β-positive cells via flow cytometry analysis. The secondary antibody labeled with fluorescein FITC was used to detect the first antibody. The stained cells were detected using a Beckman Coulter CyroFlex flow cytometer. The data were analyzed using FlowJo software version 7.6.

Cellular saturation binding and specific binding assays

A saturation binding study of Raw 264.7 cells was carried out to measure the binding affinity of radiotracers for FR. Briefly, Raw 264.7 cells (2×10^5 cells/well) were incubated in a 24-well plate with [^{131}I]IPBF or [^{131}I]IBF, ranging from 1 to 150 nM. To determine the non-specific uptake, excess FA (1 mg/mL) was added to block the FR of the cells before incubation with radiotracers. After incubation at 37 °C for 1 h, the cells were washed three times with 1 mL of PBS (pH = 7.4) and lysed with 1 mL of NaOH (1 M). The radioactivity was measured using a γ-counter. The K_d and B_{max} were calculated using GraphPad Prism software (version 7.0).

Cell uptake experiment

In the cell uptake experiment, murine Raw 264.7 cells were cultured and seeded in a 24-well plate (2.0×10^5 cells in 1 mL free-folate RPMI 1640 medium per well) to grow overnight. The radiotracer solution was diluted to 37 kBq/mL with free-folate RPMI 1640 medium, and 100 μL of the solution was added to each well. In the blocking study, the same cells were incubated with excess FA (final concentration of 100 μg/mL), and the radiotracer solution was added to each well. After incubation for different times at 37 °C, the cells were washed 2 times with cold PBS containing 0.1% bovine serum albumin and dissociated by adding 1 M NaOH. The cell suspensions were collected and the activity was measured using a γ-counter.

Animal models

Animal experiments were approved by the animal care committee of Xiamen University and carried out in compliance with the national laws related to the conduct of animal experimentation. Female wild-type (WT) C57BL/6 mice and ApoE$^{-/-}$ mice (18–20 g) were purchased from the Laboratory Animal Centre of Xiamen University. The high-fat and high-cholesterol (HFHC) diet and folate-deficient diet were obtained from Huafukang Biotechnology Co., Ltd, Beijing, China. The ApoE$^{-/-}$ mice with atherosclerotic aortas were induced by an HFHC diet for 3 and 6 months (3 and 6 M), respectively. The WT C57BL/6 mice were fed a standard chow diet and used as controls in this study.

Pathological staining and histological analysis

Pathological analysis was performed to demonstrate the histopathological characteristics of the atherosclerotic plaques and the NAFL of the ApoE$^{-/-}$ mice.

The aortas and livers of the WT and ApoE$^{-/-}$ mice (3 and 6 M) were dissected after SPECT imaging, harvested, fixed with 10% buffered formalin, dehydrated with ethanol, embedded in paraffin, and cut into seven-micrometer sections. Double-immunofluorescent staining of anti-CD68 antibody (ab31630) and anti-FOLR2 antibody (ab228643) was performed for co-localization analysis of the macrophages and FR-β in atherosclerotic plaques and fatty liver. In addition, anti-α-smooth muscle actin (α-SMA) antibody (ab32575) and anti-CD31 antibody (ab7388) were used for the co-localization of smooth muscle cells and vulnerable plaques. The sections were incubated with Alexa Fluor 488 conjugated goat anti-rabbit IgG antibody, Alexa Fluor 647

conjugated goat anti-rat IgG, or Alexa Fluor 647 conjugated goat anti-mouse IgG antibody for 1 h at room temperature. Finally, the sections were stained with DAPI, sealed with coverslips, shielded from light, and kept at 4 °C until imaging with laser-scanning confocal fluorescence microscopy. H&E staining of the aortas and liver sections was performed and imaged using a Leica DM4B microscope. ORO staining of the liver sections was performed in WT and HFHC-induced groups (3 and 6 M), respectively, and imaged with a Leica DM4B microscope.

Biodistribution

Approximately 370 kBq/100 µL of the radiotracers were diluted with PBS (pH = 7.4) and injected into C57BL/6 mice via the lateral tail vein (n = 3 in each group). The mice were sacrificed at 0.5, 1, 2, 4, 12, and 24 h post-injection (p.i.). Major organs and blood were collected, weighed, and counted in a γ-counter (Wizard 2480, Perkin-Elmer, USA). The results are listed as the percentage of the injected activity per gram (%IA/g) of tissue weight. The blood half-life ($T_{1/2z}$) of the probes was calculated according to the non-compartment model of the drug and statistics software (DAS ver2.0).

MicroSPECT imaging

In the SPECT imaging study, approximately 7.4 MBq/100 µL of radiotracer was injected via the lateral tail vein of the mouse. In vivo images were obtained at 0.5, 4, and 10 h p.i. using a preclinical scanner under general anesthesia and spontaneous breathing conditions. The WT C57BL/6 mice were used as controls. The SPECT acquisition parameters were as follows: ^{131}I (364 keV energy peak), high-energy collimators, 20% window width, 256 × 256 matrix, medium zoom, and 48 frames (nonrotational acquisition of multi-pinhole SPECT for 30 s/frame). The SPECT images were reconstructed using 3D iterative SPECT reconstruction software (Tera-Tomo^{TM}). The CT parameters were as follows: 50 kVp X-ray voltage with a 670 µA anode current and 720° projections. For the quantitation of radioactive signals in mouse aortas and other tissues, the regions of interest (ROIs) on the SPECT images were drawn and counted.

Ex vivo *autoradiography*

After SPECT imaging with [^{131}I]IPBF in the ApoE$^{-/-}$ and WT mice, ex vivo autoradiography was performed. The aortas were excised and exposed to a phosphor imaging screen for 2 h. The screen was read using a storage phosphor imager to further identify the atherosclerotic lesion uptake of the probe.

Statistical analysis

Values are expressed as mean ± SD. The student's t-test was used to compare the differences between the two different groups using GraphPad Prism software (version 7.0). Statistical significance was set at $p \leq 0.05$.

Results

Synthesis and Radiolabeling of [^{131}I]IPBF and [^{131}I]IBF

The synthesis and radiolabeling processes are illustrated in Fig. 1a. Due to the mild labeling conditions (copper-mediated cross-coupling), [^{131}I]IPBA-NHS and [^{131}I]SIB were prepared in high radiochemical yields (> 95%). The total radiochemical yields of [^{131}I]IPBF and [^{131}I]IBF were 37.83 ± 6.43% (n = 3) and 24.37 ± 2.74% (n = 3), respectively. The molar activities of [^{131}I]IPBF and [^{131}I]IBF were calculated as 6.9–17.5 MBq/nmol (n = 3) and 3.3–8.4 MBq/nmol (n = 3), respectively. As shown in Fig. 2, [^{131}I]IPBF and [^{131}I]IBF had good radiochemical purity (> 95%) and satisfactory in vitro stability after incubation in saline or PBS for 24 h. [^{131}I]IPBF has a higher lipophilicity than [^{131}I]IBF. The log P value of [^{131}I]IPBF was 1.16 ± 0.03 and that of [^{131}I]IBF was 0.52 ± 0.01.

Docking study demonstrated the highly spontaneous interaction

One goal of the present work is to evaluate the albumin-binding properties of the functional molecule, [^{131}I]IPBF (Fig. 1b). According to the modeling results of HSA with [^{131}I]IPBF and [^{131}I]IBF (Fig. 1c), the principal regions of intermolecular binding on HSA are located in hydrophobic cavities. Detailed information on the protein–ligand interactions was evaluated using the docking score. The scores for the binding of [^{131}I]IBF and [^{131}I]IPBF to HSA were calculated as − 6.839 and − 8.232, respectively. These results demonstrated that the interaction between [^{131}I]IPBF and HSA was more spontaneous than that of [^{131}I]IBF and HSA.

[^{131}I]IPBF has an eminent albumin-binding affinity

As shown in Fig. S1, in the presence of HSA, [^{131}I]IPBF could not pass through the dialysis membranes, and the downward trend of the radioactivity of the liquid in the dialysis membranes (or the upward trend in PBS) was not pronounced (about 80% retention in dialysis membranes at 24 h). For the control tracer without an albumin-binding entity ([^{131}I]IBF), the radioactivity of the liquid in the dialysis membrane declined quickly (Fig. S1a).

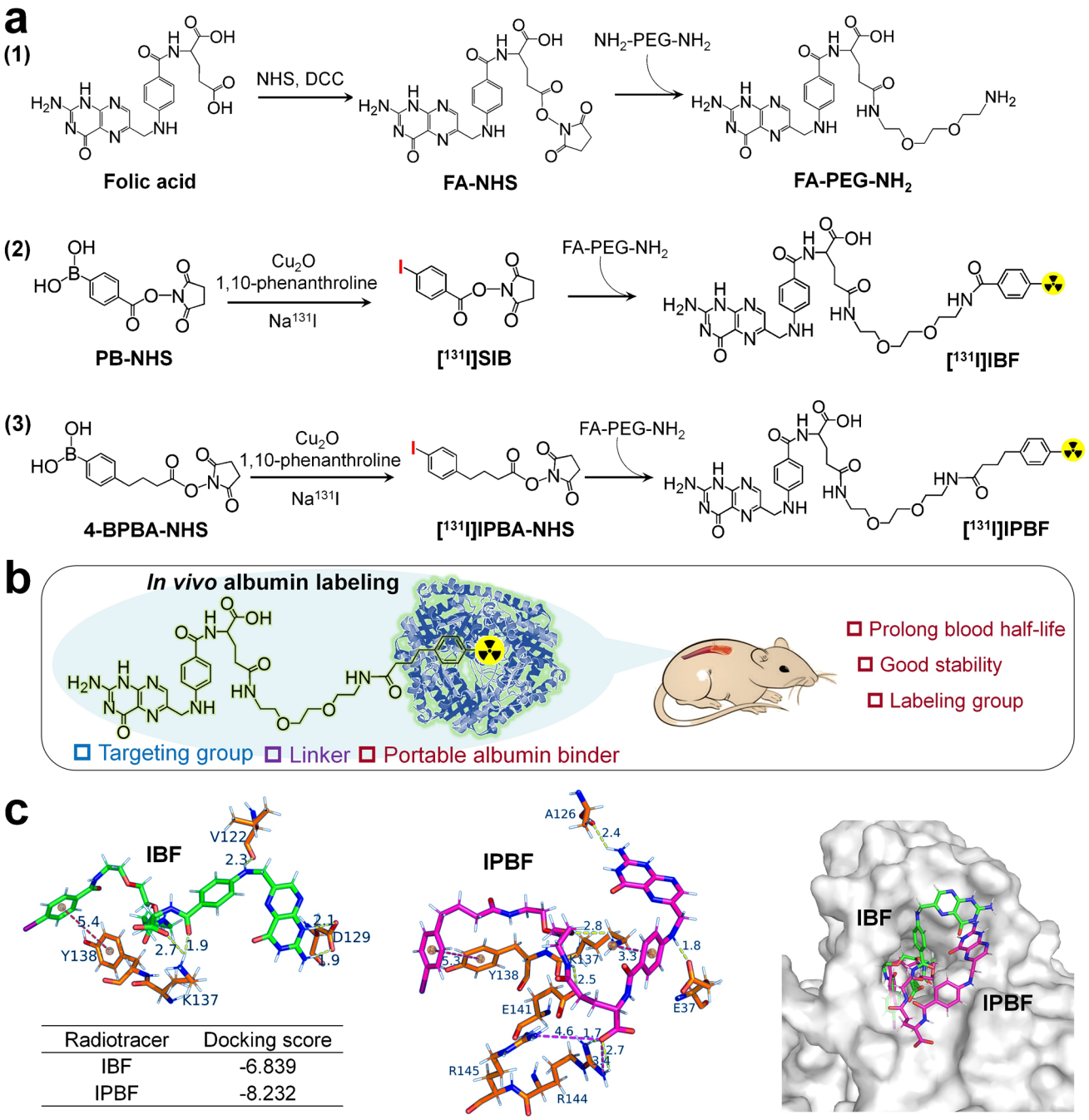

Radiotracer	Docking score
IBF	-6.839
IPBF	-8.232

Fig. 1 **a** Chemical synthesis route of [^{131}I]IBF and [^{131}I]IPBF. **b** The properties of the functional molecule, [^{131}I]IPBF. **c** Docking and score of IPBF and IBF to HSA

[^{131}I]IPBF showed an eminent albumin-binding affinity. As shown in Fig. S2. In addition, the saturation binding study of [^{131}I]IPBF to HSA indicated high albumin-affinity binding sites with K_d values of 164.50 ± 20.12 nM and B_{max} values of 8.63 ± 0.36 (× 10^5 cpm).

[^{131}I]IPBF has high specificity and affinity for FR-β

We found that red lipid droplets accumulated in normal macrophages and ox-LDL-induced macrophages were different (Fig. S3a). Macrophage foam cells are formed by an

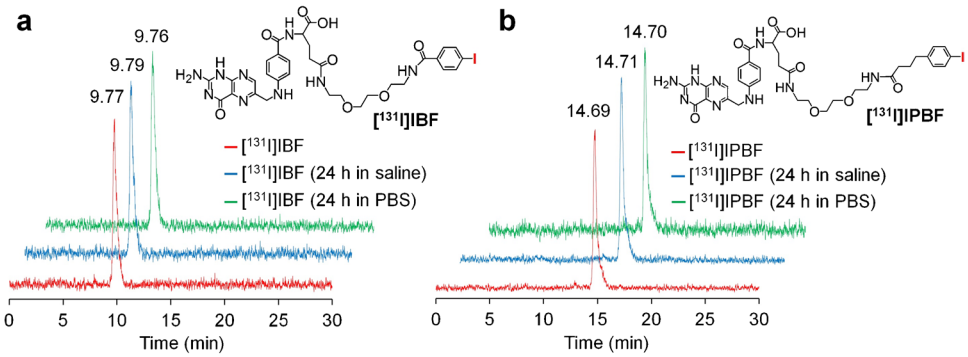

Fig. 2 Radiochemical purity of radiolabeled compounds measured by HPLC. The stability of [^{131}I]IBF (**a**) and [^{131}I]IPBF (**b**) in saline and PBS buffer (pH = 7.4) at room temperature for 24 h

imbalance of cholesterol influx, esterification, and efflux, which play a critical role in the occurrence and development of atherosclerosis. Flow cytometry analysis showed that the FR-β-positive expression of foam cells increased from 33.7 ± 6.1 to 92 ± 4.56% after incubation with ox-LDL (Fig. S3b,3c). Double-immunofluorescent staining showed that the quiescent and activated foam Raw 264.7 macrophages induced by ox-LDL expressed CD68. However, a higher expression of FR-β was detected on activated foam macrophages than quiescent macrophages (Fig. S3d).

Cell uptake experiments of [^{131}I]IPBF and [^{131}I]IBF in activated foam macrophages were performed. As shown in Fig. 3, the uptake in activated macrophages increased with incubation time. After incubation for 90 min, the uptake of radioactivity reached 12.31 ± 0.75% and 9.33 ± 0.71% of the total activity. However, the uptakes reduced to 2.53 ± 0.26% and 1.86 ± 0.32% when the macrophages were co-incubated with excess FA. This indicated that these radiolabeled folate derivatives could specifically bind with FR-β of foam cells and be blocked by excess FA.

The saturation curves of [^{131}I]IBF and [^{131}I]IPBF in the Raw 264.7 cells are shown in Fig. S4. The receptor binding affinities of [^{131}I]IBF and [^{131}I]IPBF were calculated as K_d = 61.69 ± 15.19 nM and 43.94 ± 9.83 nM, respectively. B_{max} values were 3.45 ± 0.28 and 3.07 ± 0.32 (× 10^4 cpm) for the 2 tracers, respectively.

[^{131}I]IPBF has long blood half-life and improved biodistribution

The probe function, biodistribution results, and blood clearance curves of [^{131}I]IPBF and [^{131}I]IBF are shown in Fig. 4. At 30 min p.i., [^{131}I]IPBF showed a primary distribution in the major organs, such as the liver, lung, and kidney. Radioactivity accumulation in the kidney was maintained at relatively high levels until 12 h p.i., which is directly related to the FR-mediated uptake and renal excretion pathway. Meanwhile, the radioactivities in the other organs were gradually reduced from 30 min to 24 h p.i. The thyroid had low radioactivity uptake at any observing time, which indicated that [^{131}I]IPBF has good stability in vivo. For [^{131}I]IBF, the biodistribution results showed a relatively high uptake in the kidney. The [^{131}I]IBF and [^{131}I]IPBF showed a relatively high uptake in the lung, which is due to pulmonary congestion during the operating process. And, the relatively high uptake in the stomach and intestines might be due to lipophilicity or slight deiodination. The blood elimination half-life ($T_{1/2z}$) of [^{131}I]IPBF and [^{131}I]IBF was 8.14 ± 2.56 h and

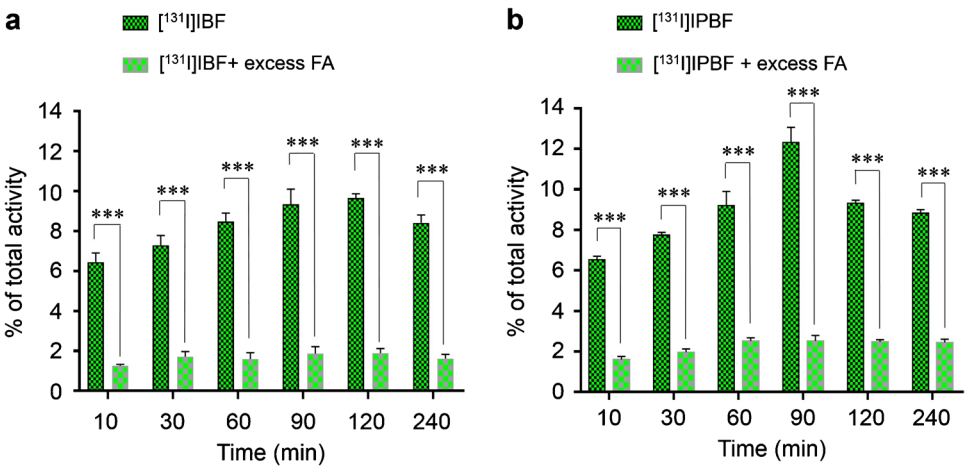

Fig. 3 Baseline and blocking experiments of [^{131}I]IBF (**a**) and [^{131}I]IPBF (**b**) in FR-β-positive activated macrophages. In the blocking study, the cells were incubated with excess FA to block FR-β on the surface. ***$p \leq 0.001$

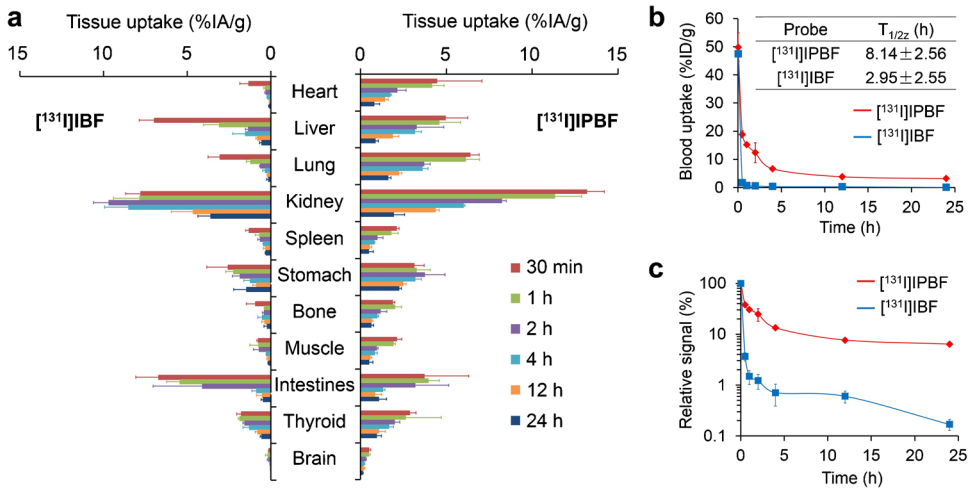

Fig. 4 **a** Biodistribution results of [^{131}I]IBF (left) and [^{131}I]IPBF (right) in C57BL/6 mice (%IA/g, mean ± SD, n = 3). Blood elimination curves (**b**) and the percentage curves (**c**) of [^{131}I]IBF and [^{131}I]IPBF

2.95 ± 2.55 h, respectively. The results demonstrated that the protein binder, IPBA, could significantly prolong the blood half-life of folate derivatives in vivo.

[^{131}I]IPBF has high uptake in AS and NAFL

As shown in Fig. 5a, the SPECT images showed that [^{131}I]IPBF targeted the vasculature of 6 M AS but not normal diet WT mice. At early time points (0.5 h p.i.), most of the radioactivity was observed in the heart (blood), liver, and kidney, resulting in an undistinguishable lesion. At 4 and 10 h p.i., benefitting from the clearance of [^{131}I]IPBF from nontarget tissues, the atherosclerotic lesions were visualized. In Fig. 5b, we contrasted the probe uptake in the arteries of different groups by drawing ROIs. Probe uptake in the inflammatory lesions of 6 M AS models was higher than that in the aortas of WT mice ($p < 0.01$), with the target/nontarget ratio (T/NT) being up to 3.71 ± 0.45 at 4 h p.i. Consistent with the SPECT imaging findings, the expression of FR-β in advanced plaques was determined by immunofluorescent staining (Fig. 5c). Pre-injection of FA as a blocking agent resulted in significant decrease of [^{131}I]IPBF uptake in FR-associated tissues (i.e., inflammatory lesions and kidneys), indicating FR-mediated uptake (Fig. 5d). As shown in Fig. 5e, SPECT imaging with [^{131}I]IPBF was used to monitor AS at an early stage. In comparison with the WT mice for the same raise period, a distinct uptake of [^{131}I]IPBF in the aortas was observed in the 3 M ApoE$^{-/-}$ atherosclerotic mice. Furthermore, we demonstrated that [^{131}I]IPBF could distinguish between different degrees of AS (Fig. 5f). As anticipated, we observed the highest radioactivity uptake of the probe in the 6 M atherosclerotic lesion, followed by the 3 M AS group. There was a significant difference in the probe uptake between the AS and WT models ($p < 0.01$).

For comparison, the disadvantages of [^{131}I]IBF with rapid blood clearance were directly reflected in the unsatisfactory imaging quality of the AS plaques. The SPECT images of [^{131}I]IBF were performed in the 6 M AS models showed a low uptake of radioactivity in the atherosclerotic lesion (Fig. S5). The rapid blood elimination of [^{131}I]IBF makes it unsuitable for targeting the FR-β of AS, which was dissuasive in our further evaluation. The results of autoradiography indicated that [^{131}I]IPBF had significant uptake in the inflammatory lesions of ApoE$^{-/-}$ AS mice induced with the HFHC diet for 6 M (Fig. 6a). For the models induced within a shorter duration (3 M), the imaging showed less radiotracer accumulation in the aortas with slight AS. In contrast, scarcely radioactive signals were observed in the aortas of the WT mice. In general, the SPECT imaging of [^{131}I]IPBF correlated significantly with the results of autoradiography in vitro.

Pathological analysis of AS identified the success of the model

As shown in Fig. 6b, ORO effectively stained neutral lipids in the atherosclerotic plaques. Immunofluorescence staining of FOLR2 showed significant FR-β expression in the inflammatory lesions of AS mice but not in that of WT mice, which was co-localized with CD68-positive macrophages (Fig. 6c). Double-immunofluorescence staining of the endothelium and α-SMA was performed to study the relative factors of plaque vulnerability. Co-localization of the α-SMA and the CD31 subset showed a type of plaque morphology that potentially advanced to rupture. Furthermore, pathological changes in the aortae were observed using the H&E staining method (Fig. 6d).

[^{131}I]IPBF could be used for imaging NAFL

To determine the association between atherosclerotic plaque and NAFL, as shown in Fig. 7a and b, the SPECT images of

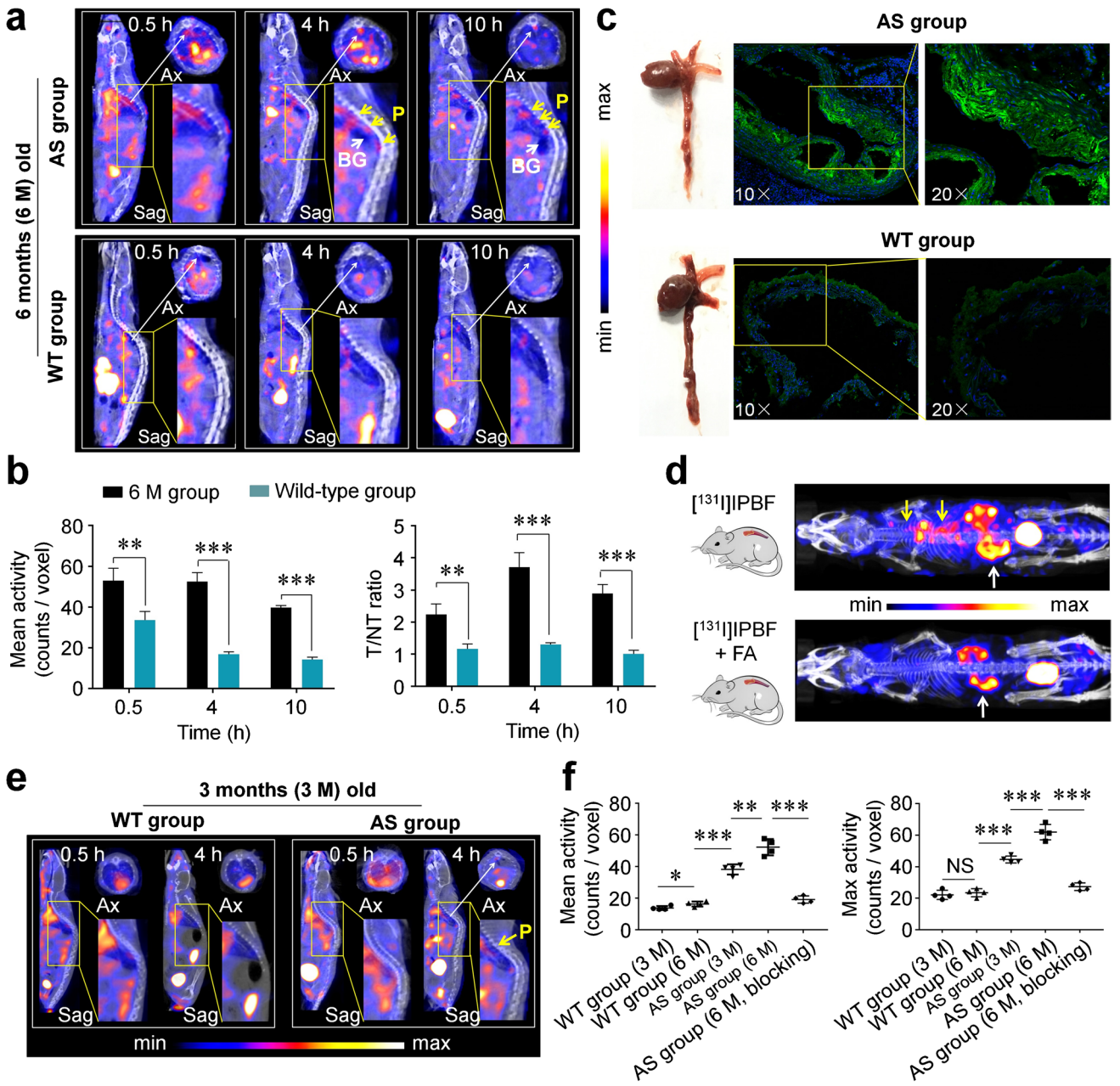

Fig. 5 **a** SPECT images (Ax and Sag) of [^{131}I]IPBF in AS (6 M) and WT mice. The plaque lesions and background selections were indicated by yellow and white arrows (P, plaque; BG, background), respectively. **b** The probe uptake of the artery and T/NT ratios in different groups were calculated by drawing ROIs on the SPECT images. **c** The anatomy of the artery in AS (6 M) and WT mice and the immunofluorescent staining of FR-β (green). The nucleus was stained with DAPI (blue). **d** MIP SPECT images of [^{131}I]IPBF in AS (6 M) mice at 4 h p.i. The blockade mouse received 100 μg native FA 10 min before the [^{131}I]IPBF administration. The yellow and white arrows point to the regions of the inflammatory component and kidney, respectively. **e** SPECT images of [^{131}I]IPBF in the AS and WT groups (3 M) at 0.5 h and 4 h p.i. **f** The mean and maximal probe uptakes of the artery in different groups at 4 h p.i. were calculated by drawing ROIs on the SPECT images. *$p \leq 0.05$; **$p \leq 0.01$; ***$p \leq 0.001$; NS, not significant

AS were further analyzed for liver-related trends. At 30 min and 4 h p.i., in vivo imaging demonstrated visible [^{131}I]IPBF uptake in the livers of 3 and 6 M HFHC diet-fed models but not in the WT mice. Significant differences in probe uptake between the AS and WT groups were observed ($p < 0.01$). The correlation analysis between arterial and hepatic uptake was performed based on the SPECT imaging findings, which indicated a significant correlation ($R^2 = 0.9843$) (Fig. 7c). After SPECT imaging, the livers were dissected and immunofluorescent staining was performed to identify

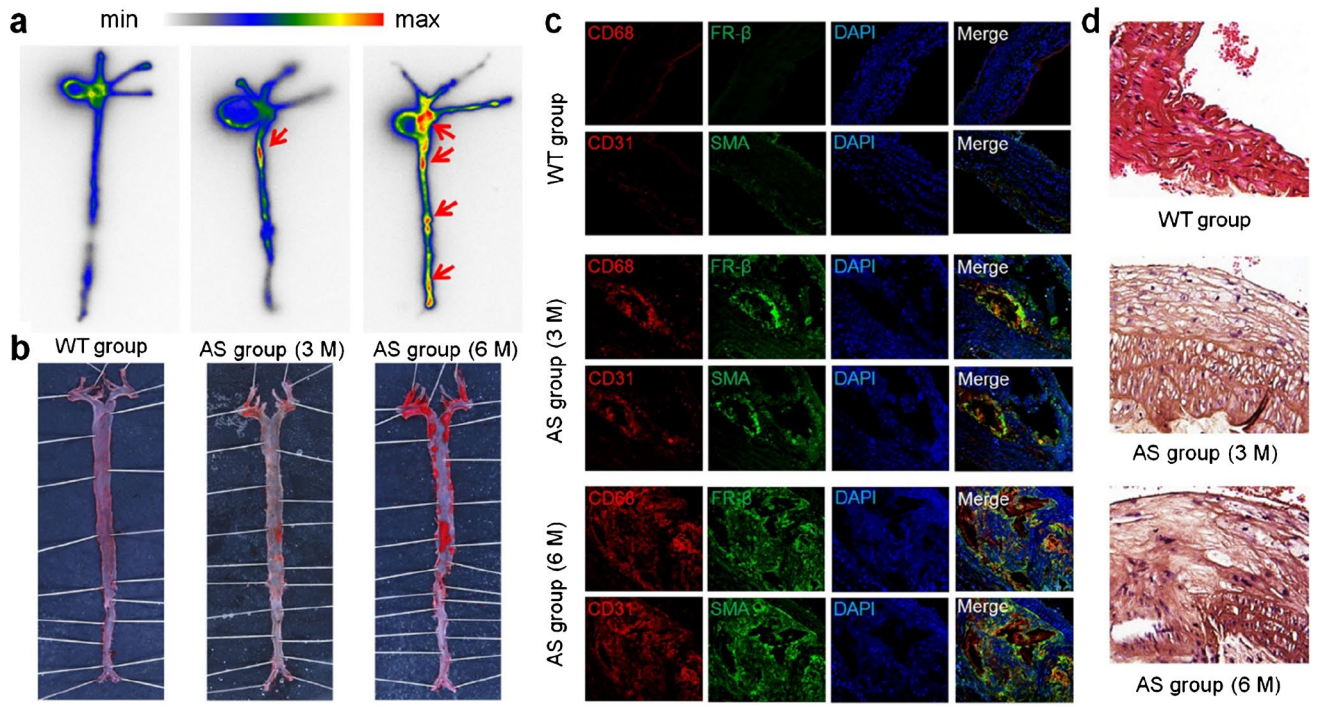

Fig. 6 **a** Autoradiography analysis of [^{131}I]IPBF distribution in the WT and AS (3 M and 6 M) mice. The lesions are indicated by the red arrows. **b** ORO staining of atherosclerosis burden in the aortic trees of WT and AS mice. **c** Co-localization of FR-β (green) vs. CD68 (red) and α-SMA (green) vs. CD31 (red) within aortic sections. **d** H&E staining of aortic sections

the expression of FR-β and CD-68 (Fig. 7d–f). Comparisons with immunofluorescence and immunohistochemical staining indicated that hepatic [^{131}I]IPBF uptake was co-localized with a higher expression of FR-β- and CD68-positive macrophages in 3 and 6 M NAFL, whereas the normal liver showed very low radioactivity and FR-β expression. H&E staining was performed to observe the pathological changes in the different groups (Fig. 7g). It is well established that the duration of induction is associated with tissue damage in the liver. In addition, ORO staining of liver sections in the WT- and HFHC-induced groups (3 and 6 M) are shown in Fig. S6. It is further confirmed that the results of ORO staining are coincident with SPECT imaging, indicating that hepatic [^{131}I]IPBF uptake is due to NAFL.

Discussion

SPECT/PET imaging with FR-β-specific probes can facilitate the detection of macrophage infiltration in AS plaques and present overall views of arterial lesions across multiple vessels. In this context, we report a novel FR-β-targeted radiotracer, [^{131}I]IPBF, with an albumin binder, which demonstrated suitable binding characteristics and good pharmacokinetics in vivo. Albumin-binding radioligands, in general, contain the following components: bifunctional chelator, albumin binder, linker, and targeting groups. In this study, [^{131}I]IPBA-NHS could serve as a Bolton-Hunter reagent and be conveniently converted into multiple molecular structures without the need for extra chelating agents. As shown in Fig. 1b, the *p*-iodophenyl moiety, [^{131}I]IPBA, performs the dual function of a labeling group and albumin-binding entity, which considerably simplifies the molecular structure of the radiotracer. This promising approach was also recommended in an inspirational study by Kelly et al., for prostate-specific membrane antigen (PSMA)-targeted radiotherapy. [41].

The choice of albumin binders was based on an optimum compromise between increased plaque uptake and low background activities as far as possible. A prolonged blood half-life would cause a high background signal of the blood pool that could decrease the T/NT ratios and influence the imaging effect. [35] Evans blue (EB) is a representative albumin-binding azo dye with high affinity. [33] However, it is likely that as a result of the prolongation of the background signal retention, there have been no reports on the feasibility of applying EB-based agents in AS imaging. The stable noncovalent binding interactions of "cold" or radioiodinated 4-(p-iodophenyl)butyric acid and HSA have been demonstrated by Neri et al. [42] and our previous research [38], respectively. Fortunately, the *p*-iodophenyl-based radiotracer, [^{131}I]IPBF, resulted in a favorable T/NT ratio and

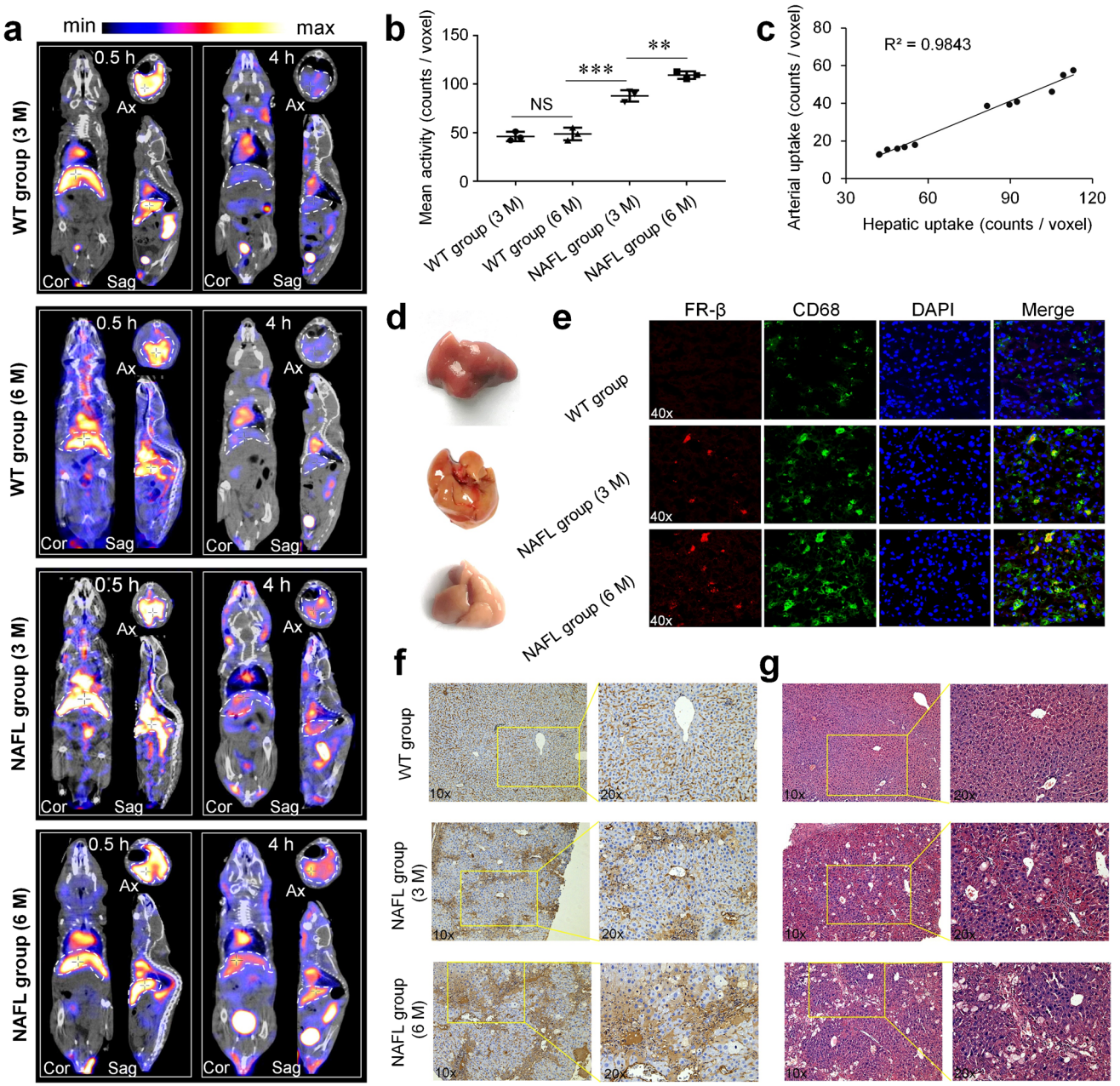

Fig. 7 **a** SPECT images (Cor, Ax, and Sag) of [^{131}I]IPBF in WT and AS (3 and 6 M) mice at 0.5 and 4 h p.i. The livers were indicated by the white dotted lines. **b** The probe uptake of the liver in different groups was calculated by drawing ROIs on the SPECT images (*$p \le 0.05$; **$p \le 0.01$; ***$p \le 0.001$; NS, not significant). **c** The correlation analysis of arterial and hepatic uptake of [^{131}I]IPBF in SPECT imaging at 4 h p.i. was performed. $R^2 = 0.9843$. **d** The anatomy of the livers from the WT mice and HFHC-induced ApoE$^{-/-}$ (3 and 6 M). **e** Immunofluorescent staining and co-localization of FR-β and CD68 in a liver section. **f**, **g** Immunohistochemical analysis for FR-β expression and H&E staining of liver biopsies

could be evaluated as a promising candidate. Compared with the non-albumin-binding radioligand [^{131}I]IBF, SPECT imaging of [^{131}I]IPBF provided higher quality images for advanced AS plaques at 4 h p.i., and it was effective even against plaques in a nascent condition with small size, which further increased the chance of early theranostics for AS.

In previous studies, radiolabeled folate derivatives (^{18}F-FOL, [^{99m}Tc]Tc-EC20, etc.) have been used to assess FR-β-positive activated macrophages, [25–28] which have an admirable targeting effect. In a rat model of autoimmune myocarditis, ^{18}F-FOL showed specific uptake in inflamed myocardium containing macrophages expressing FR-β ($SUV_{mean} = 2.1 \pm 1.1$). [28] For [^{99m}Tc]Tc-EC20, the

autoradiography showed an admirable effect. [27] However, the FR-targeted AS imaging of most folate tracers in ApoE$^{-/-}$ mice was poor for distinguishing the AS in vivo, which might result from the rapid metabolism and limited plaque uptakes. In this study, the use of a radioiodinated albumin binder improves the uptake of probe in AS plaques. With advanced modification, [^{131}I]IPBF has a commendable in vivo SPECT imaging effect for AS and can distinguish between lesions that have lasted for different durations. In this study, after a long-term western diet, some advanced lesions were observed in the aorta, and this dynamic FR-β-positive inflammation of advanced atherosclerotic plaques could be identified by SPECT imaging of [^{131}I]IPBF. Based on immunofluorescent staining, FR-β expression showed a strong correlation with macrophages and SMAs with severe inflammation in the fibrous cap, which is a type of plaque morphology (as shown in Fig. 6). The imaging of [^{131}I]IPBF can facilitate the visualization of vascular inflammation for lesion progression, severity, and destabilization, which can facilitate early diagnosis to decrease the risk of cardiovascular events. It is also worth noting that [^{131}I]IPBF has no selectivity for FR-α and FR-β. FR-α is overexpressed in a majority of cancers but restricted to normal tissues. In the follow-up experiments, we will attempt to evaluate the potential applications of [^{131}I]IPBF in the diagnosis and therapy of FR-α overexpressed tumors.

Encouraged by the satisfactory results of [^{131}I]IPBF for the imaging of FR-β-positive macrophages of atherosclerotic plaques, we speculated about the use of the radiotracer for targeting activated macrophages in NAFL. This would support further visualization of systemic metabolic syndrome and inter-organ communication based on [^{131}I]IPBF imaging, which would help us to fully understand the health status and prognostic information of patients with CVD. NAFL should be emphasized as a possible cardiac risk factor, which may predict the increased risk of CVDs, including visceral obesity, dyslipidemia, insulin resistance, and inflammation.[4, 43] To our knowledge, this is the first study to track different stages of plaques that are correlated with NAFL in a mouse model using an FR-β-targeted radiotracer with an albumin binder. Comprehensive multi-organ observation based on [^{131}I]IPBF imaging validates a strong association between AS and NAFL (Fig. 7c), which is vitally important for the effective treatment of advanced CVDs with complicated co-existing diseases. This is particularly interesting, as the current research on AS and other CVDs tends to focus on the vasculature.

We are optimistic in improving the performance of CVD agents by using this strategy. Based on the albumin-binding method of IPBA, future studies will explore the imaging agents based on radionuclide ^{124}I, because the popularity and availability of PET give ^{124}I a large advantage over the ^{131}I-labeled SPECT tracers. Also, we anticipate that the ^{18}F or ^{68}Ga will attract attention-stimulating research with a translatability to reach the clinic. Thus, the half-life of blood elimination and nuclide decay has to be carefully balanced in the design of radiotracers to reach an optimum compromise. For these short half-life nuclides, in the following research, we will select a moderate albumin binder to modify folate compounds for PET imaging, such as ibuprofen, diphenylcyclohexyl group, or fatty acid. [35, 44] We hope that moderate rather than an excessive extension of half-life could require a shorter time to achieve optimal uptake in lesion and signal to noise ratio.

Conclusion

Taken together, an FR-β targeting radiotracer ([^{131}I]IPBF) with the albumin binder was developed to detect high-risk AS plaques and NAFL in ApoE$^{-/-}$ mice. These promising albumin-binding methods and macrophage-targeted strategies would have the potential to warrant further preclinical investigations of AS plaques and concomitant fatty liver imaging.

Supplementary Information The online version contains supplementary material available at https://doi.org/10.1007/s00259-021-05447-4.

Author contributions Zhide Guo and Xianzhong Zhang were responsible for the conception and design of the study, the drafting of the manuscript, and the final approval of the version to be published. Xuejun Wen was responsible for the acquisition, analysis and interpretation of the data, and the drafting of the manuscript. Rongqiang Zhuang and Haibo Zhu contributed to critical revision for important intellectual content and final approval of the version to be published. Jinxiong Huang and Yesen Li contributed to the critical revision of the manuscript for important intellectual content and material support. Xiaoru Lin assisted in the synthesis of probes. Changrong Shi, Liu Yang, and Xinying Zeng directed the histopathological characterization of animal models.

Funding This study was financially supported by the National Natural Science Foundation of China (81901805, 21976150), Major Research Plan of the National Natural Science Foundation of China (91959122), and Joint Fund of the National Natural Science Foundation of China—China National Nuclear Corporation for Nuclear Technology Innovation (U1967222).

Declarations

Ethics approval Animal experiments were approved by the animal care committee of Xiamen University (ID XMULAC20190157) and carried out in compliance with the national laws related to the conduct of animal experimentation.

Competing interests The authors declare no competing interests.

References

1. Libby P, Ridker PM, Hansson GK. Progress and challenges in translating the biology of atherosclerosis. Nature. 2011;473:317–25.
2. Shaw L, Chandrashekhar Y. Progress in cardiovascular imaging. JACC Cardiovasc Imag. 2019;12:2589–610.
3. Nakahara T, Dweck MR, Narula N, Pisapia D, Narula J, Strauss HW. Coronary artery calcification: from mechanism to molecular imaging. JACC Cardiovasc Imag. 2017;10:582–93.
4. Lee SB, Park GM, Lee JY, Lee BU, Park JH, Kim BG, et al. Association between non-alcoholic fatty liver disease and subclinical coronary atherosclerosis: an observational cohort study. J Hepatol. 2018;68:1018–24.
5. Sinn DH, Kang D, Chang Y, Ryu S, Gu S, Kim H, et al. Non-alcoholic fatty liver disease and progression of coronary artery calcium score: a retrospective cohort study. Gut. 2017;66:323–9.
6. Sinn DH, Cho SJ, Gu S, Seong D, Kang D, Kim H, et al. Persistent nonalcoholic fatty liver disease increases risk for carotid atherosclerosis. Gastroenterology. 2017;66:323–9.
7. Ma J, Hwang SJ, Pedley A, Massaro JM, Hoffmann U, Chung RT, et al. Bidirectional analysis between fatty liver and cardiovascular disease risk factors. J Hepatol. 2017;66:390–7.
8. Makowski MR, Wiethoff AJ, Blume U, Cuello F, Warley A, Jansen CHP, et al. Assessment of atherosclerotic plaque burden with an elastin-specific magnetic resonance contrast agent. Nat Med. 2011;17:383–8.
9. Judenhofer MS, Wehrl HF, Newport DF, Catana C, Siegel SB, Becker M, et al. Simultaneous PET-MRI: a new approach for functional and morphological imaging. Nat Med. 2008;14:459–65.
10. Abele JT, Fung CI. Effect of hepatic steatosis on liver FDG uptake measured in mean standard uptake values. Radiology. 2010;254:917–24.
11. Moon SH, Hong SP, Cho YS, Noh TS, Choi JY, Kim BT, et al. Hepatic FDG uptake is associated with future cardiovascular events in asymptomatic individuals with non-alcoholic fatty liver disease. J Nucl Cardiol. 2015;24:892–9.
12. Lee HJ, Lee CH, Kim S, Hwang SY, Hong HC, Choi HY, et al. Association between vascular inflammation and non-alcoholic fatty liver disease: analysis by ^{18}F-fluorodeoxyglucose positron emission tomography. Metabolism. 2017;67:72–9.
13. Daghem M, Bing R, Fayad ZA, Dweck MR. Noninvasive imaging to assess atherosclerotic plaque composition and disease activity: coronary and carotid applications. JACC Cardiovasc Imag. 2020;13:1055–68.
14. Tabas I, Bornfeldt KE. Intracellular and intercellular aspects of macrophage immunometabolism in atherosclerosis. Circ Res. 2020;126:1209–27.
15. Kazankov K, Jørgensen SMD, Thomsen KL, Møller HJ, Vilstrup H, George J, et al. The role of macrophages in nonalcoholic fatty liver disease and nonalcoholic steatohepatitis. Nat Rev Gastroenterol Hepatol. 2019;16:145–59.
16. Park JW, Jeong G, Kim SJ, Kim MK, Park SM. Predictors reflecting the pathological severity of non-alcoholic fatty liver disease: comprehensive study of clinical and immunohistochemical findings in younger Asian patients. J Gastroenterol Hepatol. 2007;22:491–7.
17. Kelemen LE. The role of folate receptor alpha in cancer development, progression and treatment: cause, consequence or innocent bystander? Int J Cancer. 2006;119:243–50.
18. Shi H, Guo J, Li C, Wang Z. A current review of folate receptor alpha as a potential tumor target in non-small-cell lung cancer. Drug Des Devel Ther. 2015;9:4989–96.
19. O'Shannessy DJ, Somers EB, Maltzman J, Smale R, Fu YS. Folate receptor alpha (FRA) expression in breast cancer: identification of a new molecular subtype and association with triple negative disease. Springerplus. 2012;1:22.
20. Jager NA, Westra J, Golestani R, van Dam GM, Low PS, Tio RA, et al. Folate receptor-β imaging using ^{99m}Tc-folate to explore distribution of polarized macrophage populations in human atherosclerotic plaque. J Nucl Med. 2014;55:1945–51.
21. Müller A, Beck K, Rancic Z, Müller C, Fischer CR, Betzel T, et al. Imaging atherosclerotic plaque inflammation via folate receptor targeting using a novel ^{18}F-folate radiotracer. Mol Imaging. 2014;13:1–11.
22. Xia W, Hilgenbrink AR, Matteson EL, Lockwood MB, Cheng JX, Low PS. A functional folate receptor is induced during macrophage activation and can be used to target drugs to activated macrophages. Blood. 2009;113:438–46.
23. Williams JW, Giannarelli C, Rahman A, Randolph GJ, Kovacic JC. Macrophage biology, classification, and phenotype in cardiovascular disease: JACC macrophage in CVD series (part 1). J Am Coll Cardiol. 2018;72:2166–80.
24. Werner RA, Thackeray JT, Diekmann J, Weiberg D, Bauersachs J, Bengel FM. The changing face of nuclear cardiology: guiding cardiovascular care toward molecular medicine. J Nucl Med. 2020;61:951–61.
25. Paulos CM, Turk MJ, Breur GJ, Low PS. Folate receptor-mediated targeting of therapeutic and imaging agents to activated macrophages in rheumatoid arthritis. Adv Drug Deliv Rev. 2004;56:1205–17.
26. Silvola JMU, Li X, Virta J, Marjamäki P, Liljenbäck H, Hytönen JP, et al. Aluminum fluoride-18 labeled folate enables in vivo detection of atherosclerotic plaque inflammation by positron emission tomography. Sci Rep. 2018;8:9720.
27. Ayala-López W, Xia W, Varghese B, Low PS. Imaging of atherosclerosis in apoliprotein e knockout mice: targeting of a folate-conjugated radiopharmaceutical to activated macrophages. J Nucl Med. 2010;51:768–74.
28. Jahandideh A, Uotila S, Stahle M, Virta J, Li XG, Kyto V, et al. Folate receptor β-targeted PET imaging of macrophages in autoimmune myocarditis. J Nucl Med. 2020;61:1643–9.
29. Guo Z, You L, Shi C, Song M, Gao M, Xu D, et al. Development of a new FR-targeting agent ^{99m}Tc-HYNFA with improved imaging contrast and comparison of multimerization and/or PEGylation strategies for radio-folate modification. Mol Pharm. 2017;14:3780–8.
30. Guo Z, Zhang P, Song M, Wu X, Liu C, Zhao Z, et al. Synthesis and preliminary evaluation of novel ^{99m}Tc-labeled folate derivative via click reaction for SPECT imaging. Appl Radiat Isotopes. 2014;91:24–30.
31. Guo Z, Gao M, Song M, Shi C, Zhang P, Xu D, et al. Synthesis and evaluation of ^{99m}Tc-labeled dimeric folic acid for FR-targeting. Molecules. 2016;21:817–29.
32. Guo Z, Yang L, Chen M, Wen X, Liu H, Li J, et al. Molecular imaging of advanced atherosclerotic plaques with folate receptor-targeted 2D nanoprobes. Nano Res. 2019;13:173–82.
33. Lau J, Jacobson O, Niu G, Lin KS, Bènard F, Chen X. Bench to bedside: albumin binders for improved cancer radioligand therapies. Bioconjug Chem. 2019;30:487–502.
34. Siwowska K, Haller S, Bortoli F, Benešová M, Groehn V, Bernhardt P, et al. Preclinical comparison of albumin-binding radiofolates: impact of linker entities on the in vitro and in vivo properties. Mol Pharm. 2017;14:523–32.
35. Deberle LM, Benešová M, Umbricht CA, Borgna F, Büchler M, Zhernosekov K, et al. Development of a new class of PSMA radioligands comprising ibuprofen as an albumin-binding entity. Theranostics. 2020;10:1678–93.
36. Müller C, Struthers H, Winiger C, Zhernosekov K, Schibli R. DOTA conjugate with an albumin-binding entity enables the

first folic acid-targeted ^{177}Lu-radionuclide tumor therapy in mice. J Nucl Med. 2013;54:124–31.
37. Choy CJ, Ling X, Geruntho JJ, Beyer SK, Latoche JD, Langton-Webster B, et al. ^{177}Lu-labeled phosphoramidate-based PSMA inhibitors: the effect of an albumin binder on biodistribution and therapeutic efficacy in prostate tumor-bearing mice. Theranostics. 2017;7:1928–39.
38. Wen X, Shi C, Xu D, Zhang P, Li Z, Li J, et al. Radioiodinated portable albumin binder as a versatile agent for in vivo imaging with single-photon emission computed tomography. Mol Pharm. 2019;16:816–24.
39. Rios FJ, Koga MM, Pecenin M, Ferracini M, Gidlund M, Jancar S. Oxidized LDL induces alternative macrophage phenotype through activation of CD36 and PAFR. Mediators of Inflamm. 2013;2013:198193.
40. Hu Y, Wu S, Zhao J, Ma X, Lu J, Xiu J, et al. VNN1 promotes atherosclerosis progression in apoE-/- mice fed a high-fat/high-cholesterol diet. J Lipid Res. 2016;57:1398–411.
41. Kelly JM, Amor-Coarasa A, Nikolopoulou A, Wüstemann T, Barelli P, Kim D, et al. Dual-target binding ligands with modulated pharmacokinetics for endoradiotherapy of prostate cancer. J Nucl Med. 2017;58:1442–9.
42. Dumelin CE, Trüssel S, Buller F, Trachsel E, Bootz F, Zhang Y, et al. A portable albumin binder from a DNA-encoded chemical library. Angew Chem Int Ed. 2008;47:3196–201.
43. Pais R, Redheuil A, Cluzel P, Ratziu V, Giral P. Relationship among fatty liver, specific and multiple-site atherosclerosis, and 10-year framingham score. Hepatol. 2019;69:1453–63.
44. Höltke C, Grewer M, Stölting M, Geyer C, Wildgruber M, Helfen A. Exploring the influence of different albumin binders on molecular imaging probe distribution. Mol Pharm. 2021. https://doi.org/10.1021/acs.molpharmaceut.1c00064.

Authors and Affiliations

Xuejun Wen[1] · Changrong Shi[1] · Liu Yang[2] · Xinying Zeng[1] · Xiaoru Lin[1] · Jinxiong Huang[3] · Yesen Li[3] · Rongqiang Zhuang[1] · Haibo Zhu[2] · Zhide Guo[1] · Xianzhong Zhang[1]

[1] State Key Laboratory of Molecular Vaccinology and Molecular Diagnostics & Center for Molecular Imaging and Translational Medicine, School of Public Health, Xiamen University, 4221-116 Xiang'An South Rd, Xiamen 361102, China

[2] State Key Laboratory for Bioactive Substances and Functions of Natural Medicines, Beijing, Key Laboratory of New Drug Mechanisms and Pharmacological Evaluation Study, Institute of Materia Medica, Chinese Academy of Medical Sciences & Peking Union Medical College, Beijing 100050, China

[3] Department of Nuclear Medicine & Minnan PET Center, Xiamen Cancer Hospital, The First Affiliated Hospital of Xiamen University, Teaching Hospital of Fujian Medical University, Xiamen 361003, China